Tuning optical absorption of SnO by isoelectronic alloying for PV absorber

Haowei Peng,* Andiry Zakutayev, and Stephan Lany

National Renewable Energy Laboratory, Golden, CO 80401, USA

Abstract

Tin mono-oxide, SnO, is an excellent bi-polar oxide with both high hole and electron mobility. However the strongly indirect band gap prevents its application for photovoltaic absorbers. In this work, we explored the energetics and electronic structures of cation-site isoelectronic alloyed SnO. We found that alloying with Mg, Zn, Ca, and Sr with a composition around 10% is quite promising to significantly improve the prospect of SnO as a photovoltaic absorber.

PACS numbers:

All-oxide solar cell is a promising concept of next-generation photovoltaics (PV), due to its potential for large-scale production by easy-to-scale manufacturing methods. [1] Towards its realization, finding a high-efficiency oxide PV absorber is the key step. Currently the most popular oxide PV absorber is Cu_2O, which suffers from the relatively large band gap. [1] An efficient PV absorber material requires a complicated set of both intrinsic and extrinsic properties, including the suitable band gap, good optical absorption within the visible optical spectrum, high carrier mobilities, controllable p-type or n-type doping, etc.. SnO, which crystalizes in the tetragonal PbO layered structure,[2–4] excellently satisfies the requirements for the mobility and bi-polar dopability.[5, 6] By contrast, most common oxides possess a relatively heavy hole effective mass, as well as an excellent but exclusively n-type conductivity.

To achieve good p-type properties, researchers have considered Cu(I)-, Ag(I)-, Mn(II)-based oxides, [7–9] or other transition-metal-based oxides,[10] utilizing the p–d coupling within the valence band. The p–d coupling can lead to a valence band maximum characterized of an anti-bonding state, which is usually higher in energy (facilitating p-type doping and defect tolerance),[11] and is more dispersive (indicating a lower hole effective mass). [12] As an example, a reasonable 6% efficiency has been achieved in a Cu_2O solar cell. [13] Similar to hybrid organic-inorganic lead-halide perovskites,[14–16] in SnO, the s–p coupling between Sn and O takes the role of p–d coupling in those transition-metal oxides, [17] and the averaged band-curvature hole effective mass [12] goes down to around $0.5\,m_0$ along the c-direction according to our density functional theory (DFT) calculation within the generalized gradient approximation (GGA). [18] As for the bipolar conduction, SnO can demonstrate intrinsic p-type conduction, as well as n-type conduction via Sb-doping,[19, 20] with the origin mentioned above thoroughly discussed with several combined theory and experimental work. [21, 22] The electron effective mass of SnO is comparable with traditional n-type transparent conducting oxides, i.e., around $0.3\,m_0$.

Unfortunately, the pristine SnO is a strongly indirect band gap semiconductor: its fundamental band gap is of 0.7 eV with the valence band maximum (VBM) at Γ-point and the conduction band maximum (CBM) at M-point of the tetragonal Brillouin zone, while the optical band gap is about 2.7 eV attributed to the direct transition at Γ-point. [23] For PV absorbers, the fundamental band gap, E_g, determines the upper limit of the open circuit voltage, V_{OC}, and the optical absorption is directly related to the efficiency of sunlight

harvesting, and therefore the short circuit current, J_{SC}. An ideal PV absorber material should have the same energy for both the two gaps, together with a sharp onset of optical absorption. Hence tuning the band structure of SnO to bring together its fundamental band gap and optical band gap is technically very attracting.

In this work, we will show the effects of cation-site isoelectronic alloying on reducing the difference of the two band gaps in SnO. Using first-principles calculations, we explored the electronic structure and optical properties of (Sn, M)O alloys with M including Mg, Ca, Sr, and Zn. The cation-site alloying weakens the original Sn–O and Sn–Sn connection, opening the fundamental band gap. Meanwhile, it reduces the symmetry, allowing for optical transition between the valence band conduction bands with a smaller energy separation. Accompanying these improvement, the good properties of the pristine SnO, such as the light effective masses, have been preserved. We found that cation-site alloying with a composition around 10% is quite promising to tailor SnO as a PV absorber, which makes all-oxide-based solar cell feasible.

We have considered alloying SnO with Mg, Ca, Sr, and Zn, with compositions of 3.125%, 6.25%, 12.5%, and 25%. To model the alloy structures, we employed the special quasi-random structures (SQS) [24, 25] as generated with the *mcsqs* utility as implemented in ATAT. [26] The SQS method allows us to model the fully random alloys with a relatively small supercell, and the 256-atom supercells were chosen which enable the resulting SQSs to have the pair correlation functions agree with the ideal random alloys even beyond the 8th nearest neighbour of the cation sublattice for all compositions considered. To further take into account the nature of random alloying, four different SQSs for each composition were implemented, and the averaged quantities were reported in the following. To facilitate the Brillouin zone sampling during the DFT calculations, we have chosen the supercells with a shape close to a cube.

The first-principles calculations were performed the projector augmented wave (PAW) method [27] as implemented in the VASP code. [28–30] The SQSs were fully relaxed with the GGA in the standard Perdew-Burke-Ernzerhof(PBE) formalism, [31] with a $2 \times 2 \times 2$ Monkhost-Pack k–mesh, [32] during which an on-site Coulomb correction, $U = 6\,\mathrm{eV}$, was applied on the Zn-3d states. With the relaxed SQSs, the modified Becke-Johnson local density approximation (MBJ-LDA) [33] was utilized to calculate the electronic structure, as well as the optical absorption spectrum. MBJ-LDA is a potential-based meta-GGA

functional, which uses the modified Becke-Johnson exchange potential together with the LDA correlation. With the MBJ-LDA functional, one can obtain the band gaps close to high-level GW methods at a computational cost comparable to standard DFT calculations. [34–36] A $3 \times 3 \times 3$ Monkhost-Pack k–mesh was employed for the MBJ-LDA calculations. Based on the electronic structure and optical absorption spectrum [37] results from MBJ-LDA, we can assess the theoretical efficiency for these alloys to be used as PV absorbers. Instead of the well-known Shockley-Queisser (SQ) limit,[38] we calculated the so-called Spectroscopic Limited Maximum Efficiency (SLME). [39] Compared to the ideal SQ limit, which only takes the band gap as the single material-related parameter, the SLME also includes the finite absorbance of a film with a certain thickness, which is very important for SnO-based alloys due to the indirect-gap nature and the slow absorption onset.

FIG. 1. (Color online) The calculated mixing energies, ΔE_{Mix}, per formula unit for $Sn_{1-x}M_xO$ alloys with $0.03125 \leq x \leq 0.25$.

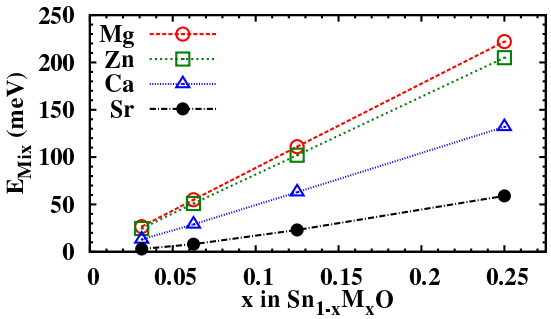

First, we calculated the mixing energies of the (Sn, M)O alloys with M = Mg, Zn, Ca, and Sr. The mixing energy, ΔE_{Mix}, was defined as

$$\Delta E_{Mix} = E(Sn_{1-x}M_xO) - (1-x)E(SnO) - xE(MO), \quad (1)$$

with $E(SnO)$ and $E(MO)$ calculated from their ground-state structure. The calculated mixing energy as a function of composition for all alloys are shown in Fig. 1. As found in other heterostrctural alloys, [40] the mixing energy increases almost linearly with the composition. Such linear relation suppresses the spinodal decomposition, enhancing the chances to grow a homogeneous alloy by overcoming the binodal miscibility gap via non-equilibrium techniques. [40, 41] The mixing energy decreases from Mg-, Zn-, Ca-, to Sr-alloyed systems. We related such trend to the ionic size mismatch. To compare the ionic radii of those ions with the same

coordination environment, instead of the Shannon ionic radii, [42] we directly use the M–O bond-length in the rocksalt structure from first-principles calculations. We found the M–O bond length is 2.12, 2.12, 2.35, 2.60, and 2.56 Å for Mg, Zn, Ca, Sr, and Sn, respectively. Assuming the Shannon Radii for O^{2-} (coordination number = 6) of 1.40 Å,[42] the ionic radii for those cations are 0.72, 0.72, 0.95, 1.20, and 1.14, respectively. Note that the ionic radii obtained in this way for the cations other than Sn^{2+} agrees with the values tabulated by Shannon within 0.05 Å. [42] Further considering the layer structure of SnO, where Sn^{2+} has a stereoactive lone pair pointing to the space between the Sn-O layers, [4] Sn^{2+} here should have an even larger effective ionic radii. Hence, the ionic radii mismatch decrease along the sequence of Sr–Ca–Zn–Mg, along which the mixing energy increases. From the calculations, we would expect that it is easier to growth the Sr- and Ca-alloyed samples, and the Mg- and Zn-alloyed samples are still possible with a composition smaller than 10% with the non-equilibrium techniques. [40, 41]

FIG. 2. (Color online) The calculated total density of states (DOS), and site-projected DOS for SnO (a), and (Sn, M)O with a composition of 12.5% (b). Since the total DOS is very similar for all the alloys, only that for (Sn, Zn)O was shown in (b). For clarification, density of states per atom was plotted, and the valence band maxima are set to energy zero.

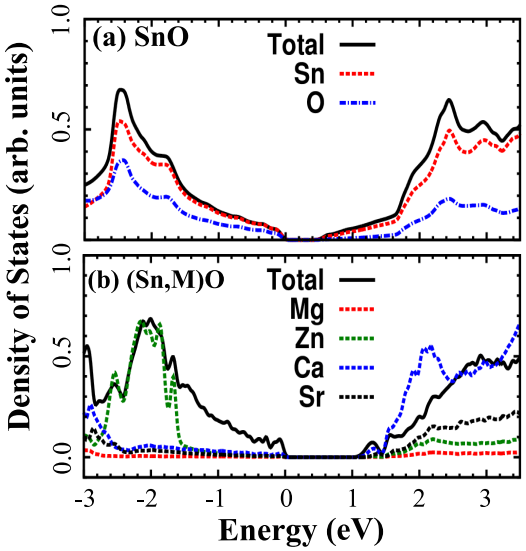

In Fig. 2, we plotted the density of states (DOS), as well as the site-projected DOS for SnO, and (Sn, M)O alloys with a composition of 12.5%. In SnO, the Sn-5s, and Sn-5p orbital

dominate respectively the DOS near the VBM and CBM, [17] distinguishing it from other main group oxides that typically have O-p orbitals in the valence band and metal-s orbitals in the conduction band. Replacing 12.5% Sn with other cations, we can see the band gap opens, and the density of states was renormalized especially near the CBM. However, the extrinsic cations do not have significant contribution to the DOS near the band edges. For example, the Zn-3d states are mainly located around 1.5 eV below the VBM, and Mg has neglectable contribution for the whole energy range in the figure. Hence we argue that the effects of alloying on the electronic structure and optical properties are mainly through reducing the symmetry of the pure SnO, and weakening the original Sn–O and Sn–Sn network. As a result, we should not find strong chemical dependence of the electronic structure and optical absorption spectrum on the alloying element (Zn, Sr, Ca, Mg) as described below.

TABLE I. The calculated electron, and hole density of states (DOS) effective masses, m^e_{DOS} and m^h_{DOS}, of the (Sn, M)O alloys compared with SnO. The unit is electron rest mass m_0.

	m^e_{DOS} (m_0)				m^h_{DOS} (m_0)			
x	Mg	Zn	Ca	Sr	Mg	Zn	Ca	Sr
$\frac{0}{128}$		0.4				0.9		
$\frac{4}{128}$	0.5	0.5	0.5	0.4	1.2	1.2	1.2	1.2
$\frac{8}{128}$	0.5	0.5	0.6	0.7	1.3	1.3	1.3	1.3
$\frac{16}{128}$	0.6	0.6	0.6	0.7	1.5	1.5	1.6	1.4
$\frac{32}{128}$	1.1	1.1	1.3	1.8	2.1	2.1	2.0	1.9

While no defect-like state within the band gap was identified from the DOS plots, the renormalization near the band edges raises a concern whether the charge carrier effective masses becomes significant heavier than the pristine SnO. To explore the effects of isoelectronic alloying on the carrier mobility, we calculated the DOS effective mass, m^e_{DOS} and m^h_{DOS}, as tabulated in Table I. The DOS effective mass is a suitable quantity to describe the mobility for the large low-symmetry supercell calculations here.[9] The hole DOS effective mass is defined by the relation [8]

$$m^{h\,\frac{3}{2}}_{DOS} \propto N_v(T) = \int_{-\infty}^{E_{VBM}} D(E) \times exp[(E - E_{VBM})/k_B T]dE, \tag{2}$$

and similarly, for the electron DOS effective mass,

$$m_{DOS}^{e\,\frac{3}{2}} \propto N_c(T) = \int_{E_{CBM}}^{\infty} D(E) \times exp[(E_{CBM} - E)/k_B T]dE. \tag{3}$$

Here, $D(E)$ denotes the DOS, $N_v(T)$ and $N_c(T)$ are the temperature-dependent effective density of states for the valence and conduction band, respectively. For a single parabolic band, $N_{c/v}(T) = 2(\frac{2\pi m_{DOS}^{e/h} k_B T}{h^2})^{\frac{3}{2}}$. Here the temperature $T = 900\,K$ was chosen which gives more reliable results due to the finite k-mesh used for the large supercell. As shown in Table I, both the hole and electron effective masses of the alloys only slightly increase when the composition is not larger than 0.125. By contrast, the results for all alloys with $x = 0.25$, a big jump shows up for both the hole and electron effective masses. We have checked the wavefunctions of the VBM and CBM states for this high-composition alloys, and found that the both the VBM and CBM state tend to localize on the Sn-rich regions (yet not overlapping with each other). We attribute this to the breakdown of the Sn–O–Sn network by the high composition alloying.

FIG. 3. (Color online) The fundamental band gap, E_g, and optical band gap, E_g^O, calculated from MBJ-LDA for the Zn-, Mg-, Ca-, and Sr-alloyed SnO. The optical band gap is defined as the energy where the calculated optical absorption coefficient becomes larger than $10^3 cm^{-1}$.

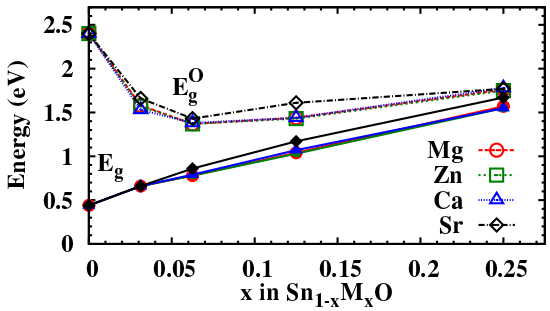

In Fig. 3, we compared the fundamental band gap, E_g, and optical band gap, E_g^O, obtained from the MBJ-LDA calculations, for all the alloy systems considered in this study. During this calculation, the phonon-assistant indirect absorption, and the excitonic effect, were not taken into account, which can usually enhance noticeably the optical absorption near the absorption edge.[37] For convenience, we define the optical band gap, E_g^O, as the

energy at which the optical absorption coefficient, α, becomes larger than a threshold value for which a value of $10^3 cm^{-1}$ was chosen in this study. To put this definition into the context, E_g^O for GaAs from a similar calculation here, is about 0.2 eV larger than the fundamental band gap E_g. As shown in the figure, all alloys share the same trends for the two band gaps as a function of the alloy composition, and the difference between different extrinsic cations is very small as already discussed before. The fundamental band gap always increases with the composition within the range considered, while the optical band gap first decreases dramatically and then increases follow the fundamental band gap. The dramatic decrease in the optical band gap upon 3.125% doping ($E_g^O = 2.4eV$ for SnO), indicates the more fundamental effect of the symmetry-reducing arising from alloying. From Fig 3, our investigation predict a sweet spot around the composition of 12%, at which the fundamental band gap is around 1.0 eV on the MBJ-LDA level, and the indirectness ΔE_g is less than 0.4 eV as compared to 2.0 eV for SnO.

FIG. 4. (Color online) The calculated effective band structure of the $Sn_{1-x}Zn_xO$ alloys, with (a) $x = 0.0625$, and (b) $x = 0.125$. For comparison, we plot the band structure of pristine SnO with white dashed line on top of the effective band structure. The energy of valence band maximum of both SnO, and $Sn_{1-x}Zn_xO$ alloys are set to zero.

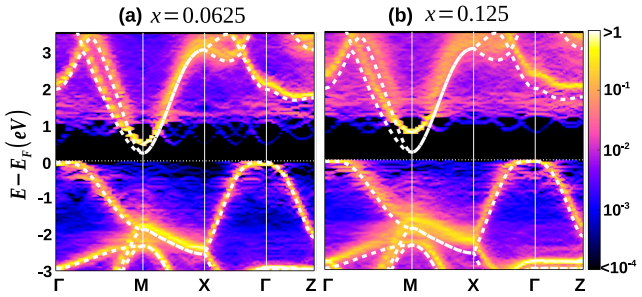

To see how alloying actually modifies the band structure, we plotted the "effective band structure" for the $Sn_{120}Zn_8O_{128}$, and $Sn_{112}Zn_{16}O_{128}$ alloys, as shown in Fig. 4.[43] In these plots, we show with a color scale the spectral function $A(\vec{k}; E)$:

$$A(\vec{k}; E) = \sum_i |\left\langle \Psi_{i\vec{K}} | \vec{k} \right\rangle|^2 \delta(\epsilon_i - E), \tag{4}$$

where $\vec{k}$ ($\vec{K}$) denotes Bloch wave vectors of SnO primitive cell and the SQS supercell, $\Psi_{i,\vec{K}}$ is the eigenstate of the supercell with the eigenvalue of ϵ_i, and the spectral weight $|\langle \Psi_{i\vec{K}} | \vec{k} \rangle|^2$

describes the projection of the supercell eigenstate onto the basis of the Bloch states in the reciprocal space of the primitive cell.[43] Carefully choosing the $\vec{K}$ vectors, we can unfold the dispersion, $\epsilon_i(\vec{K})$, of the SQS supercell along the high-symmetry $\vec{k}$-points, i.e., the so-called effective band structure. The unfolding has been performed using the BandUP code.[44] For comparison, we also plotted the band structure of the pristine SnO on top of the effective band structure of the alloys, with the valence band maxima set to energy zero. From this direct comparison, we found that the general features, as well as the backbone of the band structure of the pristine SnO were well preserved in the alloys. The brightest points of the effective band structure (highest spectrum function) indicate the indirect fundamental band gap from Γ to M, the same as the pristine SnO. The fundamental band gap increases apparently with the composition of Zn here. More importantly, new states, as illustrated as the pink region, show up in the SQS supercell with their energies close to the band edges. Such states contribute to low-energy direct band-to-band absorption which does not present in the pristine SnO. Comparing the two plots, we found the spectrum function of these states also goes up with the composition of Zn. As a result, the fundamental band gap of the alloys becomes larger than SnO, and the optical absorption will start almost immediately at the fundamental band gap with a slope depending on the composition. Another important point which is already shown in Fig. 2, the isoelectronic alloying does not introduce in-gap defect-like states.

FIG. 5. (Color online) The calculated spectroscopic limited maximum efficiency (SLME, open circles) assuming a thin film with a thickness of 2 μm, compared with the Shockley-Queisser limit (SQ, full square) for the alloys. For comparison, we also give the SLME for Cu_2SnZnS_4, denoted with the horizon dashed line.

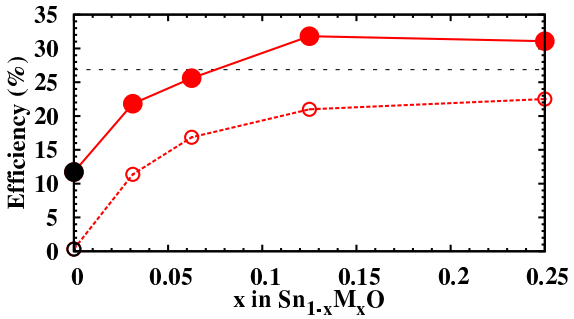

To have a more straight-forward understanding the effects of tuning the shape of the band structure by alloying on the performance of SnO as a PV absorber, we calculated the SLME assuming a thickness of $2\,\mu m$, as shown in Fig. 5. Since the band gaps, optical absorption spectra, and hence the SLME, are very similar for all the alloy systems, we only shown the average value in the figure. First, we found that even the smallest alloying composition considered here enhance the efficiency from zero to 11%. Second, the SLME curve becomes quite flat after 10% of alloying, which suggest that we have quite a large optimal area to prepare the SnO-based alloys for PV absorber. To highlight the importance of the detailed shape of band structure, and hence the optical absorption spectrum, we also compared the SLME with the SQ limit, the latter of which simply assume the absorption spectrum with a step-function. Not surprising, the SLME is always smaller than the SQ limit. We also calculated the SLME for Cu_2SnZnS_4 (CZTS) based on GW calculation, and found that the performance of SnO-based alloys is actually comparable with the CZTS device.

In summary, we performed first-principles calculations of the energetics, and effects of tuning the shape of the band structure of SnO by isoelectroic alloying. We found that alloying with Mg, Zn, Ca, and Sr with a composition around 10% is quite promising to significantly improve the prospect of the bi-polar SnO as a photovoltaic absorber.

This work is supported by the U.S. Department of Energy, Office of Science, Office of Basic Energy Sciences, Energy Frontier Research Centers, under Contract No. DE-AC36-08GO28308 to NREL. The high performance computing resources of the National Energy Research Scientific Computing Center and of NRELs Computational Science Center are gratefully acknowledged.

* Haowei.Peng@gmail.com

[1] S. Rühle, A. Y. Anderson, H. N. Barad, B. Kupfer, Y. Bouhadana, E. Rosh-Hodesh, and A. Zaban, J. Phys. Chem. Lett. **3**, 3755 (2012).

[2] G. W. Watson, J. Chem. Phys. **114**, 758 (2001).

[3] A. Walsh and G. Watson, J. Phys. Chem. B **109**, 18868 (2005).

[4] A. Walsh, D. J. Payne, R. G. Egdell, and G. W. Watson, Chem. Soc. Rev. **40**, 4455 (2011).

[5] Y. Ogo, H. Hiramatsu, K. Nomura, H. Yanagi, T. Kamiya, M. Hirano, and H. Hosono, Appl.

Phys. Lett. **93**, 032113 (2008).

[6] Y. Ogo, H. Hiramatsu, K. Nomura, H. Yanagi, T. Kamiya, M. Kimura, M. Hirano, and H. Hosono, Phys. Status Solidi **206**, 2187 (2009).

[7] H. Kawazoe, M. Yasukawa, and H. Hyodo, Nature **389**, 939 (1997).

[8] G. Trimarchi, H. Peng, J. Im, A. Freeman, V. Cloet, A. Raw, K. Poeppelmeier, K. Biswas, S. Lany, and A. Zunger, Phys. Rev. B **84**, 165116 (2011).

[9] H. Peng, A. Zakutayev, S. Lany, T. R. Paudel, M. D'Avezac, P. F. Ndione, J. D. Perkins, D. S. Ginley, A. R. Nagaraja, N. H. Perry, T. O. Mason, and A. Zunger, Adv. Funct. Mater. **23**, 5267 (2013).

[10] T. R. Paudel, S. Lany, M. Avezac, A. Zunger, N. H. Perry, A. R. Nagaraja, T. O. Mason, J. S. Bettinger, Y. Shi, and M. F. Toney, Phys. Rev. B **84**, 064109 (2011).

[11] A. Zakutayev, C. M. Caskey, A. N. Fioretti, D. S. Ginley, J. Vidal, V. Stevanovic, E. Tea, and S. Lany, J. Phys. Chem. Lett. **5**, 1117 (2014).

[12] G. Hautier, A. Miglio, G. Ceder, G.-M. Rignanese, and X. Gonze, Nat. Commun. **4**, 2292 (2013).

[13] T. Minami, Y. Nishi, and T. Miyata, Appl. Phys. Express **8**, 022301 (2015).

[14] M. A. Loi and J. C. Hummelen, Nat. Mater. **12**, 1087 (2013).

[15] F. Hao, C. C. Stoumpos, D. H. Cao, R. P. H. Chang, and M. G. Kanatzidis, Nat. Photonics **8**, 489 (2014).

[16] F. Brivio, K. Butler, A. Walsh, and M. V. Schilfgaarde, Phys. Rev. B **89**, 155204 (2014), arXiv:arXiv:1401.6993v1.

[17] A. Walsh and G. Watson, Phys. Rev. B **70**, 235114 (2004).

[18] a. Togo, F. Oba, I. Tanaka, and K. Tatsumi, Phys. Rev. B **74**, 195128 (2006).

[19] K. Nomura, T. Kamiya, and H. Hosono, Adv. Mater. **23**, 3431 (2011).

[20] L. Y. Liang, Z. M. Liu, H. T. Cao, W. Y. Xu, X. L. Sun, H. Luo, and K. Cang, J. Phys. D. Appl. Phys. **45**, 085101 (2012).

[21] N. F. Quackenbush, J. P. Allen, D. O. Scanlon, S. Sallis, J. a. Hewlett, A. S. Nandur, B. Chen, K. E. Smith, C. Weiland, D. a. Fischer, J. C. Woicik, B. E. White, G. W. Watson, and L. F. J. Piper, Chem. Mater. , 130705123622004 (2013).

[22] J. P. Allen, D. O. Scanlon, F. J. Piper, and G. W. Watson, J. Mater. Chem. C **1**, 8194 (2013).

[23] H. Hosono, Y. Ogo, H. Yanagi, and T. Kamiya, Electrochem. Solid-State Lett. **14**, H13

(2011).

[24] A. Zunger, S. Wei, L. Ferreira, and J. Bernard, Phys. Rev. Lett. **65**, 353 (1990).

[25] S. H. Wei, L. G. Ferreira, J. E. Bernard, and A. Zunger, Phys. Rev. B **42**, 9622 (1990).

[26] A. Van de Walle, P. Tiwary, M. de Jong, D. Olmsted, M. Asta, A. Dick, D. Shin, Y. Wang, L.-Q. Chen, and Z.-K. Liu, Calphad **42**, 13 (2013).

[27] P. Blöchl, Phys. Rev. B **50**, 17953 (1994).

[28] G. Kresse and J. Hafner, Phys. Rev. B **49**, 14251 (1994).

[29] G. Kresse and J. Furthmüller, Phys. Rev. B **54**, 11169 (1996).

[30] G. Kresse and D. Joubert, Phys. Rev. B **59**, 1758 (1999).

[31] J. P. Perdew, K. Burke, and M. Ernzerhof, Phys. Rev. Lett. **77**, 3865 (1996).

[32] H. Monkhorst and J. Pack, Phys. Rev. B **13**, 5188 (1976).

[33] D. Koller, F. Tran, and P. Blaha, Phys. Rev. B **85**, 155109 (2012).

[34] D. Singh, Phys. Rev. B **82**, 205102 (2010).

[35] D. Koller, F. Tran, and P. Blaha, Phys. Rev. B **83**, 195134 (2011).

[36] J. a. Camargo-Martínez and R. Baquero, Phys. Rev. B **86**, 195106 (2012).

[37] M. Gajdoš, K. Hummer, G. Kresse, J. Furthmüller, and F. Bechstedt, Phys. Rev. B - Condens. Matter Mater. Phys. **73**, 1 (2006).

[38] W. Shockley and H. J. Queisser, J. Appl. Phys. **32**, 510 (1961).

[39] L. Yu and A. Zunger, Phys. Rev. Lett. **108**, 068701 (2012).

[40] H. Peng, P. F. Ndione, D. S. Ginley, A. Zakutayev, and L. S, Phys. Rev. X (Accepted).

[41] a. Zakutayev, V. Stevanovic, and S. Lany, Appl. Phys. Lett. **106**, 123903 (2015).

[42] R. D. Shannon, Acta Crystallogr. Sect. A (1976), 10.1107/S0567739476001551.

[43] V. Popescu and A. Zunger, Phys. Rev. Lett. **104**, 236403 (2010).

[44] P. V. C. Medeiros, S. Stafström, and J. Björk, Phys. Rev. B **89**, 041407 (2014).